

## Effect of surface roughness on heat transfer in Rayleigh-Bénard convection

Tummers, Mark J.; Steunebrink, Martin

**DOI**

[10.1016/j.ijheatmasstransfer.2019.05.066](https://doi.org/10.1016/j.ijheatmasstransfer.2019.05.066)

**Publication date**

2019

**Document Version**

Final published version

**Published in**

International Journal of Heat and Mass Transfer

**Citation (APA)**

Tummers, M. J., & Steunebrink, M. (2019). Effect of surface roughness on heat transfer in Rayleigh-Bénard convection. *International Journal of Heat and Mass Transfer*, 139, 1056-1064. <https://doi.org/10.1016/j.ijheatmasstransfer.2019.05.066>

**Important note**

To cite this publication, please use the final published version (if applicable). Please check the document version above.

**Copyright**

Other than for strictly personal use, it is not permitted to download, forward or distribute the text or part of it, without the consent of the author(s) and/or copyright holder(s), unless the work is under an open content license such as Creative Commons.

**Takedown policy**

Please contact us and provide details if you believe this document breaches copyrights. We will remove access to the work immediately and investigate your claim.



# Effect of surface roughness on heat transfer in Rayleigh-Bénard convection



Mark J. Tummers\*, Martin Steunebrink

Delft University of Technology, Faculty of Mechanical, Maritime and Materials Engineering, Mekelweg 2, 2628 CD Delft, the Netherlands

## ARTICLE INFO

### Article history:

Received 2 January 2019

Received in revised form 14 May 2019

Accepted 21 May 2019

Available online 1 June 2019

### Keywords:

Rayleigh-Bénard convection

Natural convection

Heat transfer enhancement

Surface roughness

Thermochromic liquid crystals

Particle image velocimetry

## ABSTRACT

This paper reports on an experimental study of the effects of surface roughness on the flow and heat transfer in cubical Rayleigh-Bénard convection cells for Rayleigh numbers between  $10^7$  and  $10^{10}$ . In the rough cells the top and bottom surfaces are equipped with square arrays of copper cubes. In line with other studies, three different regimes occur in the rough cells, with each regime having a different relation between the Nusselt number,  $Nu$ , and the Rayleigh number,  $Ra$ . In the first regime the  $Nu$ - $Ra$  relation equals that of the smooth cell, but in the second and third regimes the  $Nu$ - $Ra$  relation deviates from that of the smooth cell with significantly higher Nusselt numbers. To better understand these observations, the flow and temperature fields in both the smooth and rough cells were visualised by using particle image velocimetry with suspended thermochromic liquid crystals as flow tracer particles.

© 2019 The Authors. Published by Elsevier Ltd. This is an open access article under the CC BY license (<http://creativecommons.org/licenses/by/4.0/>).

## 1. Introduction

Rayleigh-Bénard (R-B) convection is the fluid flow in the space between two horizontal walls where the fluid is heated from below and cooled from above. Many researchers have studied this system using convection cells with different geometries and different working fluids. The case with smooth horizontal walls is well documented in a large number of papers reporting on numerical and/or experimental studies. For an overview the reader is referred to Ahlers et al. [1], Lohse et al. [2], and Chillà and Schumacher [3]. Some studies focus on the characteristics of the temperature and flow fields inside the cell, but the most frequently studied topic is the relation between the Nusselt number ( $Nu$ ) and the Rayleigh number ( $Ra$ ), which represent the dimensionless heat transfer and the dimensionless buoyancy, respectively. Great efforts have been made to theoretically describe this aforementioned relation between the Nusselt number and the Rayleigh number, see Grossmann and Lohse [5] and Stevens et al. [4].

In an interesting variation on the standard type of R-B convection cells with smooth walls, ordered structures are mounted on the upper and/or lower walls, giving rise to so-called rough cells. It has been shown that the heat transfer can be significantly increased when the roughness elements on the conducting plates have proper characteristics, see for instance Du and Tong [6]. This

effect of wall roughness on heat transfer in natural convection may be of interest to practical applications such as electronics cooling where heat produced by electronic components must be removed to prevent the occurrence of hot spots, or in meteorology where surface boundaries are usually not smooth.

Several other studies have addressed the effects of rough upper and lower surfaces on R-B convection. It has been reported that heat transfer increases in rough cells (with respect to smooth cells) when the thermal boundary layer thickness  $\delta_0$  becomes less than the roughness height  $h$ . If the Rayleigh number is increased beyond this point, some researchers have observed a short transition to a regime where the Nusselt number is increased (compared to the smooth case) with a constant factor, i.e., the pre-factor  $a$  in the relation  $Nu = aRa^\gamma$  is larger than in the corresponding smooth case, see for instance Shen et al. [7], Du and Tong [6]. Qiu et al. [8] conducted experiments in a cylindrical cell and reported on an increase in both the pre-factor and the scaling exponent due to the rough wall. Others have reported on a change of the value of the exponent  $\gamma$  only (Roche et al. [9], Tisserand et al. [10]). Ciliberto and Laroche [11] considered roughness elements in the form of glass spheres (with relatively low thermal conductivity) which were glued to the surface with thermal conductive paint. They measured a lower Nusselt number with respect to the smooth case, although with a higher value of the exponent  $\gamma$ . Villermaux [12] proposed a model that predicts a modest increase ( $\sim 10\%$ ) of value of  $\gamma$  for irregular surface roughness while the value of the exponent remains the same for regular roughness elements.

\* Corresponding author.

E-mail address: [m.j.tummers@tudelft.nl](mailto:m.j.tummers@tudelft.nl) (M.J. Tummers).

Experiments by Xie and Xia [13] in a cylindrical cell with rough top and bottom walls (with pyramid-shaped roughness elements) indicated the existence of three regimes. A first regime in which the relation between the Nusselt number and the Rayleigh number is the same as in the case of smooth walls, a second regime with an increased exponent, and a third regime also with an increased exponent, but its value is generally somewhat lower than in the second regime. Rusaouën et al. [14] carried out experiments in a cylindrical R-B cell with one smooth and one rough wall (with cubical roughness elements) that confirmed the existence of these three regimes.

Shishkina and Wagner [15] carried out 2D numerical simulations for cases with a small number of relatively large rectangular roughness elements and found an increase of the exponent. The DNS study by Wagner and Shishkina [16] showed that the increase of the exponent depends on the geometry and spacing of the roughness elements, and that for increasing Rayleigh numbers the value of the exponent becomes similar to that for the smooth walls.

Zhu et al. [17] carried out a DNS of Taylor-Couette flow with grooved walls and found that the power law relation between the dimensionless torque and the Taylor number (which are the analogues of dimensionless heat transfer and Rayleigh number, respectively) also has three characteristic regimes depending on the whether the boundary layer thickness (which depends on the Taylor number) is larger or smaller than the groove height.

This study focuses on the effect of (well conducting) ordered surface roughness on the flow field and the heat transfer in cubical R-B convection cells. The objective is to determine the  $Nu$ - $Ra$  relation for this type of roughness, and to find out if there are specific processes occurring within the rough cells that are responsible for the heat transfer enhancement. For this purpose, two smooth and three rough cubical R-B convection cells were built. The two smooth cells have different heights to increase the Rayleigh number range considered in this study. The three rough cells have different ratios of roughness height and cell height.

## 2. Experimental setup

### 2.1. Rayleigh-Bénard convection cells

The characteristics of the different cells that are used in this study are listed in Table 1. All five cells are (nearly) cubical with inner dimension  $H$ . Fig. 1a shows a vertical cross section of a smooth cell (left) and a cell with surface roughness (right). Each cell consist of copper top and bottom plates and the side walls are made of 2 mm thick glass. The roughness elements on the top and bottom plates are small copper cubes with dimensions  $h \times h \times h$ . The cubes are arranged as a square array with a pitch of  $2h$ , as illustrated in Fig. 1b. The distance between the top and bottom plates in the rough cells,  $\hat{H}$ , is made slightly larger than that of the corresponding smooth cells,  $H$ , because the cubical roughness elements protrude into the cell. The relation between these two heights is:

$$\hat{H} = H + h/2. \quad (1)$$

**Table 1**  
Characteristics of the five R-B cells. The height of the cubical roughness elements is  $h$ .

Cell description	$h$ [mm]	$H$ [mm]
Small smooth	0	77
Small rough 1 mm	1	77
Small rough 3 mm	3	77
Large smooth	0	155
Large rough 3 mm	3	155

By adjusting the physical height,  $\hat{H}$ , of the rough cell according to Eq. (1) the surface-averaged height of the rough cell equals the height of the smooth cell. As a consequence, the liquid volumes in both cells are equal.

The top and bottom plates of each cell are equipped with a number of epoxy coated NTC thermistors of type C100 (General Electric). The relation between the temperature and resistance in the range  $273.15 \text{ K} < T < 323.15 \text{ K}$  is specified by the manufacturer as:

$$T^{-1} = a_1 + a_2 \ln\left(\frac{R_{th}}{R_{25}}\right) + a_3 \left(\ln\left(\frac{R_{th}}{R_{25}}\right)\right)^2 + a_4 \left(\ln\left(\frac{R_{th}}{R_{25}}\right)\right)^3$$

where  $a_1 = 3.354 \times 10^3 \text{ K}^{-1}$ ,  $a_2 = 2.562 \times 10^{-4} \text{ K}^{-1}$ ,  $a_3 = 2.082 \times 10^{-6} \text{ K}^{-1}$ ,  $a_4 = 7.300 \times 10^{-8} \text{ K}^{-1}$ ,  $R_{th}$  is the electrical resistance of the thermistor at temperature  $T$  (in K) and  $R_{25}$  is the electrical resistance of the thermistor at 298.15 K. The value of  $R_{25}$  differs for each thermistor but is usually somewhere between  $9900 \Omega$  and  $10100 \Omega$ . The individual thermistors are calibrated by measuring the value of  $R_{25}$  when the thermistors are positioned inside the copper plates. A Pt100 thermometer with an inaccuracy of 0.05 K is used as the temperature standard during the calibration.

Water from a thermostatic circulator flows through a brass plate that is mounted on the top copper plate (see Fig. 1a) to keep this top plate at a pre-set constant temperature. The convection cells are heated from below with electrical heating foils that are attached to the bottom of the lower plate. The heating foils have dimensions  $80 \times 80 \text{ mm}^2$ , so the small cells are equipped with one foil and the large cells with four foils. The cells are fully covered in a 3 cm thick layer of insulating foam, insuring that the heat produced in the heating foils per unit time  $Q$  equals the heat transfer rate through the fluid. The heat flux,  $q$ , through the cell is calculated from  $q = Q/H^2$ . The heat transfer rate  $Q = I\Delta V$  is determined by measuring the total electrical current  $I$  and the voltage difference  $\Delta V$  at the electrical connections near the heating foils. The Nusselt number is then computed as  $Nu = q H/(k \Delta T)$  where  $k$  is the thermal conductivity of the working fluid and  $\Delta T$  is the temperature difference between the bottom and top walls of the cell. The effect of the conduction through the vertical side walls of the cell was estimated using the procedure proposed by Roche et al. [18] and found to have negligible effect on the Nusselt number. In this study the Rayleigh number is computed as  $Ra = \beta g \Delta T H^3/(\nu\alpha)$  where  $g$  is the gravitational acceleration,  $\beta$  is the thermal expansion coefficient,  $\nu$  is the kinematic viscosity, and  $\alpha$  is the thermal diffusivity of the working fluid. Finally, the Prandtl number is defined as  $Pr = \nu/\alpha$ . For the highest Rayleigh numbers considered in each measurement series, the uncertainty of the measured Rayleigh- and Nusselt numbers are determined as  $\Delta Ra/Ra = 1.9\%$  and  $\Delta Nu/Nu = 1.5\%$ .

### 2.2. TLC and PIV measurements

The flow tracer particles used in this research are encapsulated Thermochromic Liquid Crystals (TLCs) with a mean diameter of about  $25 \mu\text{m}$ . The encapsulated TLC particles are illuminated by a “white” light sheet that is constructed as follows. Light from a Waldman MCXFL3S light emitting diode is focused onto a glass fibre bundle that is connected to a line light (Schott Fostec) producing a homogeneous light intensity along its length. The light coming from the line light is then focused into a vertical sheet that spans the height of the cell by using a cylindrical lens.

The encapsulated TLC particles are of type R25C60W and produced by Hallcrest. The red start temperature of  $25 \text{ }^\circ\text{C}$  and the temperature bandwidth of  $60 \text{ }^\circ\text{C}$  are both specified by the manufacturer, and refer to a situation where the viewing angle (i.e. the angle between the incident white light and the recorded

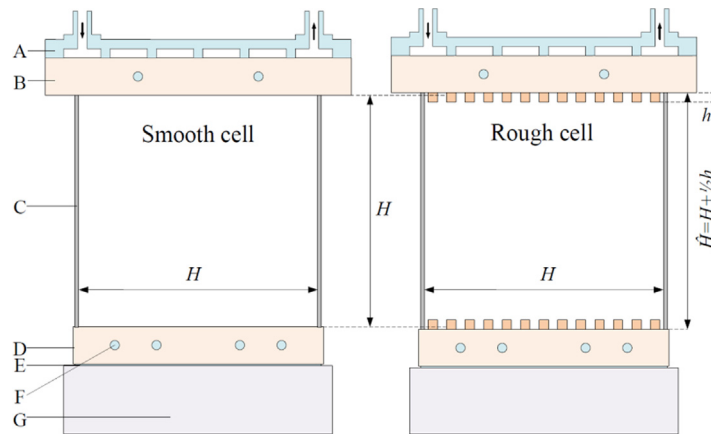


**Fig. 1a.** R-B cells with smooth walls (left) and rough walls (right). A = hollow brass plate, B = top copper plate, C = glass side wall, D = copper bottom plate, E = electrical heating foil, F = thermistor (6×); G = bottom insulation plate.

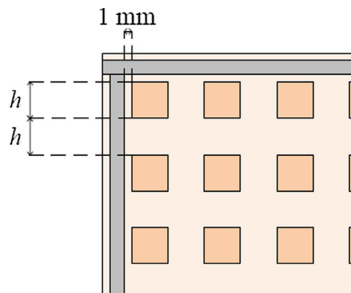


**Fig. 1b.** Top view of the square array with cubical roughness elements.

reflected light) is  $180^\circ$ . In the present experiment the light reflected by the TLC particles is collected in a direction normal to the light sheet so that the viewing angle is  $90^\circ$ . For that viewing angle the red start temperature and bandwidth are reduced to about  $19.7^\circ\text{C}$  and  $8.6^\circ\text{C}$ , respectively. The scattered light from encapsulated TLC particles was recorded by a PCO SensiCam SVGA camera with a  $2/3''$  CCD sensor with  $1280 \times 1024$  pixels. The camera was equipped with a Nikon lens with 55 mm focal length and numerical aperture of 2.8. A background image was created by determining, for each pixel, the minimum intensity value in the series of 25,000 images. This background image was subsequently subtracted from each individual image. The commercial software DaVis was used for analyzing the image pairs and vector calculation. The image pairs were processed in two consecutive steps with decreasing interrogation area size. In the first step, interrogation areas of  $16 \times 16$  pixels were cross-correlated. The resulting particle displacements were used as window displacements for a cross correlation with interrogation areas of  $8 \times 8$  pixels corresponding to  $0.67 \times 0.67 \text{ mm}^2$  in physical space. A local median filter was employed to remove spurious vectors during the iterative processing and the resulting empty spaces were filled by interpolated vectors. Based on the guidelines described in Adrian and Westerweel [19], the uncertainty of the velocity vectors was approximately 3% of the maximum velocity in the convection cells.

In this study the encapsulated TLC particles are used as both temperature indicators and flow tracers. The hydrodynamic response time  $t_h$  of a spherical particle can be determined from:

$$t_h = \rho_p d^2 \left( 1 + \frac{1}{2} \rho_f / \rho_p \right) / 18\mu$$

where  $d$  and  $\rho_p$  are the diameter and the density of the particle, respectively, and  $\mu$  and  $\rho_f$  are the dynamic viscosity and the density

of the fluid, respectively. The term inside the brackets stems from the added mass of a spherical particle [20]. The density of the encapsulated liquid crystals is close to that of water, but typically a bit higher, i.e.,  $\rho_p$  varies between  $1.00 \times 10^3 \text{ kg/m}^3$  and  $1.02 \times 10^3 \text{ kg/m}^3$  [21]. For the larger particles in the liquid crystal samples ( $d = 50 \mu\text{m}$ ) with the highest density ( $\rho_p = 1.02 \times 10^3 \text{ kg/m}^3$ ) the response time is  $t_h = 0.22 \text{ ms}$ , which is sufficiently small to follow the velocity fluctuations in the flow considered in this study. The settling velocity of a  $50 \mu\text{m}$  particle in water, as determined from  $V_s = (\rho_p - \rho_f)gd^2/18\mu$ , equals  $V_s = 0.028 \text{ mm/s}$  which is negligible compared to the typical velocities found in the convection cells in this study. The thermal response time of the encapsulated liquid crystals cannot be determined easily, but for chiral-nematic liquid crystals the response time is relatively small, i.e., in the order of several milliseconds (Dabiri [21], Abdullah et al. [22]). Günther and Rudolf von Rohr [23] have reported a thermal response time of 1 ms for Hallcrest encapsulated liquid crystals of type R25C20W with a mean diameter of  $19 \mu\text{m}$  which is similar to the encapsulated liquid crystals used in the present study.

### 2.3. Working fluids

Four different working fluids (water, methanol, ethanol and acetone) were used to extend the Rayleigh number range that can be obtained for a particular cell. All experiments were conducted with the bulk temperature of the fluid nearly equal to room temperature to minimize the driving force for heat transfer between the R-B cell and its surroundings. The thermo-physical properties of the four working fluids were determined in the temperature range between 293 K and 298 K (by using the Dortmund Data Bank) to enable accurate calculation of the Rayleigh, Prandtl and Nusselt numbers at the actual bulk temperature. The actual room temperature varied slightly from day to day, but at a mean value of 295 K the Prandtl numbers of water, methanol, ethanol and acetone were determined as 6.7, 7.6, 17.0 and 4.2, respectively.

### 2.4. Experimental program

The study considered three types of surfaces (smooth, 1 mm roughness and 3 mm roughness), two cell sizes (77 mm height (small cell) and 155 mm height (large cell)) and four working fluids. In total twelve different experiments were conducted, and these are listed in Table 2. In the following sections different experiments will be referred to as, for example, “small/smooth/water” meaning that the experiment is conducted in the small R-B cell

**Table 2**  
List of experiments.

Exp.#	Cell description	Fluid
1	Small smooth	Water
2	Small smooth	Ethanol
3	Large smooth	Water
4	Large smooth	Methanol
5	Small rough 1 mm	Water
6	Small rough 1 mm	Ethanol
7	Small rough 1 mm	Methanol
8	Small rough 3 mm	Water
9	Small rough 3 mm	Methanol
10	Small rough 3 mm	Acetone
11	Large rough 3 mm	Water
12	Large rough 3 mm	Methanol

with 77 mm height and smooth walls while the working fluid is water.

**3. Results**

*3.1. Experiments in the smooth R-B cells*

Experiments 1–4 were conducted in the smooth cells, see Table 2 for details. As an illustration, Fig. 2a shows the Nusselt number  $Nu$  as a function of the Rayleigh number  $Ra$  for experiments in the small smooth cell for both water and ethanol. For each experiment the data points were least-squares fitted to the functional form  $Nu = aRa^\gamma$ . The resulting lines have nearly identical slope and the corresponding value of the exponent was (for all four experiments in the smooth cell) determined as  $\gamma = 0.294$ . This value compares very well to the value of  $\gamma = 0.297$  that was reported by Xia et al. [24] for measurements in a (cylindrical) water filled cell at a similar range of Rayleigh numbers. Fig. 2b shows  $NuRa^{-0.294}$  as a function of the Rayleigh number, and the results indicate that small jumps occur between the four groups of data points. These jumps are mainly due to the differences in Prandtl number of the working fluids, and Fig. 2c shows that this mild Prandtl number dependence can be absorbed by the inclusion of the term  $Pr^{-0.05}$ , consistent with the findings of Xia et al. [24]. The Prandtl-number-corrected Nusselt number, defined as  $Nu^* = NuPr^{-0.05}$ , is then determined as

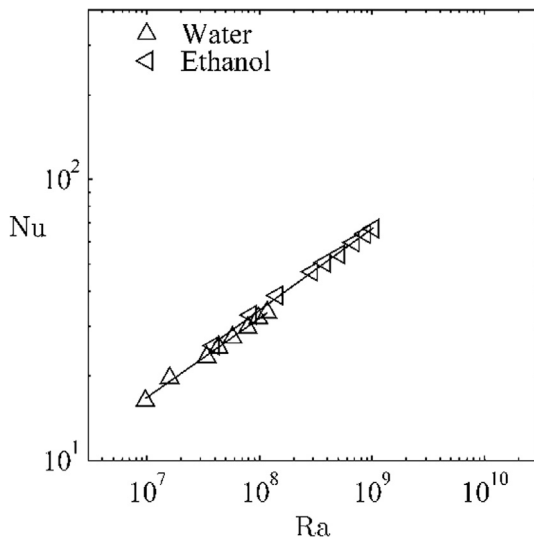


**Fig. 2a.**  $Nu$  as a function of  $Ra$  for experiments in the small smooth cell for both water and ethanol (experiments 1 and 2).

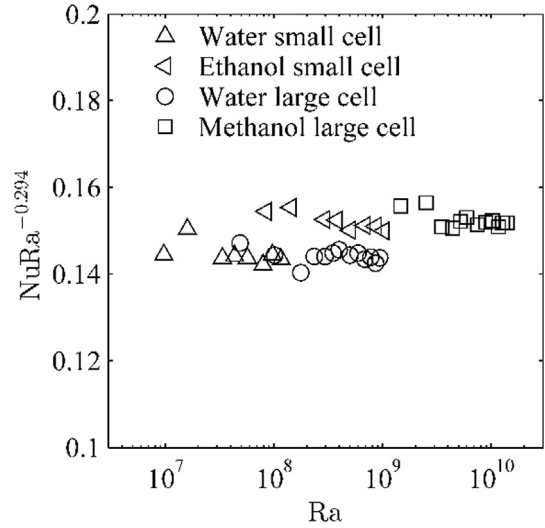


**Fig. 2b.**  $NuRa^{-0.294}$  as a function of  $Ra$  for experiments 1, 2, 3 and 4.

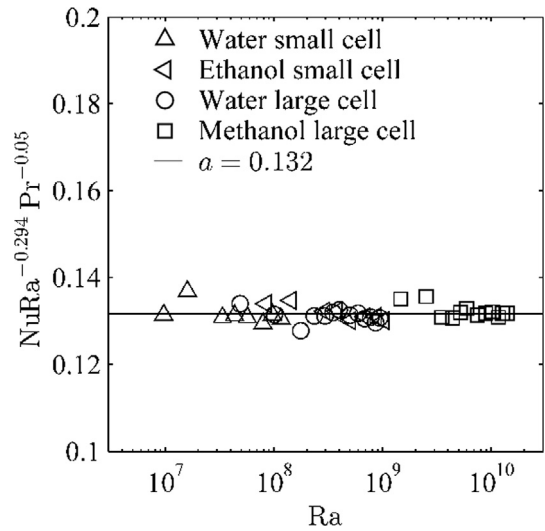


**Fig. 2c.**  $NuRa^{-0.294}Pr^{-0.05}$  as a function of  $Ra$  for data shown in Fig. 2b.

$$Nu^* = 0.132Ra^{0.294} \tag{2}$$

and shown as a solid line in Fig. 2d together with all data points from the four experiments in the smooth cell. The  $Nu$ - $Ra$  relation given by Eq. (2) will serve as a reference in the comparison with the results for the experiments in the rough cells.

*3.2. Effects of the wall roughness*

Experiments 5–12 are conducted in the cells with rough surfaces, see Table 2. The results of these experiments are presented in Figs. 3a, 3b and 3c. The data in Figs. 3a and 3b pertain to equal cell height, but different roughness heights, while the data in Figs. 3b and 3c pertain to equal roughness height, but different cell heights. The solid line represents the correlation for the Nusselt number determined for the smooth wall, Eq. (2). It can be observed in Figs. 3a, 3b and 3c that roughness elements in the form of copper cubes have a very significant effect on the heat transfer in the cell. The graphs indicate that the  $Nu^*$  values for the rough cells start to deviate from those of the smooth cells at different Rayleigh numbers. This is usually explained (see Du and Tong [6] and Shen et al. [7]) by assuming that the roughness starts to have an effect

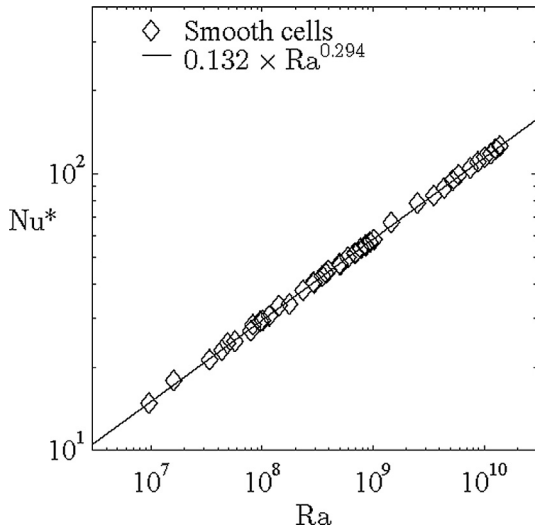


Fig. 2d.  $Nu^*$  as a function of  $Ra$  for all experiments together with the correlation.  $Nu^* = 0.132Ra^{0.294}$ .

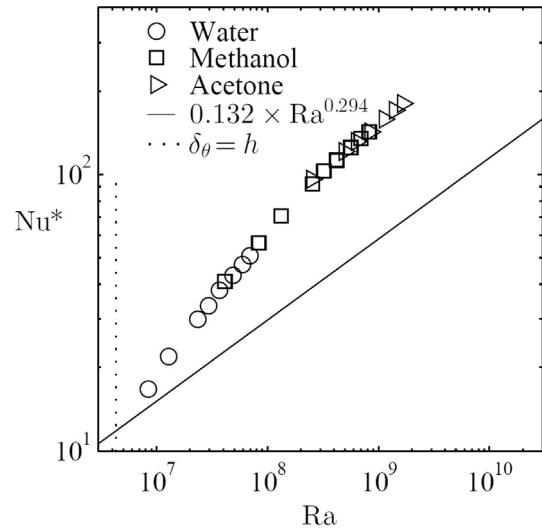


Fig. 3b.  $Nu^*$  as a function of  $Ra$  for the small cell with 3 mm roughness elements. The vertical dotted line denotes  $Ra = Ra_{low}$  according to Eq. (3) for  $Pr = 6.7$  (water).

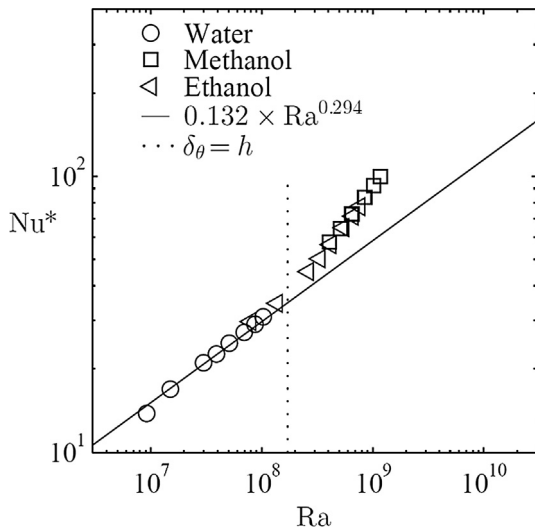


Fig. 3a.  $Nu^*$  as a function of  $Ra$  for the small cell with 1 mm roughness elements. The vertical dotted line denotes  $Ra = Ra_{low}$  according to Eq. (3) for  $Pr = 6.7$  (water).

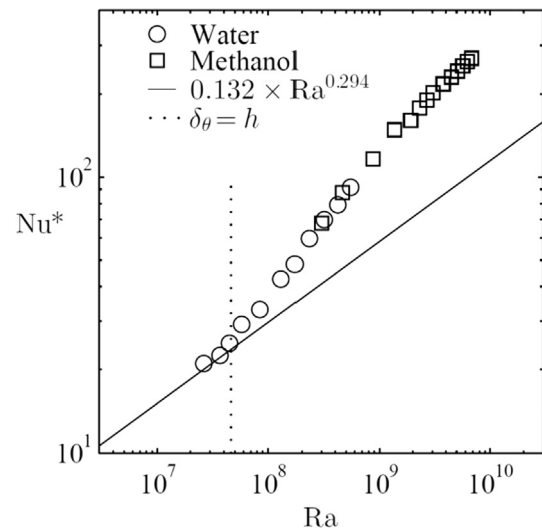


Fig. 3c.  $Nu^*$  as a function of  $Ra$  for the large cell with 3 mm roughness elements. The vertical dotted line denotes  $Ra = Ra_{low}$  according to Eq. (3) for  $Pr = 6.7$  (water).

when the thermal boundary layer thickness  $\delta_\theta$  is approximately equal to the height of the surface roughness  $h$ , i.e., when  $\delta_\theta = h$ . The corresponding Rayleigh number,  $Ra_{low}$ , is calculated by using the relation  $\delta_\theta = H/(2Nu)$  (see Belmonte et al. [25]) together with the  $Nu$ - $Ra$  relation given by Eq. (2) as:

$$Ra_{low} = \left( \frac{H}{2ahPr^{0.05}} \right)^{\frac{1}{\gamma}} \quad (3)$$

Note that the results in Fig. 3a do not show evidence of a lowering of the Nusselt number just before the transition at  $Ra = Ra_{low}$  as was observed in experiments by Tisserand et al. [10] and in the results of numerical simulations by Stringano et al. [26].

Figs. 3b and 3c also indicate that at higher Rayleigh numbers, the  $Nu$ - $Ra$  relations for both the small and large cells with 3 mm roughness, tend to approach an asymptote that has the same (or very similar) slope as that found for the smooth cells, but with a higher pre-factor. The  $Nu$ - $Ra$  relation for the rough cells apparently equals that for the smooth case for low Rayleigh numbers ( $Ra < Ra_{low}$ ) and after a transition to a region with a higher exponent ( $\gamma = \gamma_2 \approx 0.54$ ), the  $Nu$ - $Ra$  relation becomes parallel to that

for the smooth case but with a pre-factor equal to  $2.7a$  instead of  $a$ . The value of  $2.7$  in the pre-factor is interesting in the sense that it is larger than the ratio of the surface areas of the rough and smooth walls, which in the present study equals  $A_{rough}/A_{smooth} = 2$ .

The  $Nu$ - $Ra$  relation for rough surfaces is qualitatively sketched in Fig. 3d where the Rayleigh number range is divided into three regimes. For the present experiments, the first regime (smooth regime) and the third regime both have the same exponent  $\gamma_1 = \gamma_3 = \gamma = 0.294$  with pre-factors  $a_1 = a = 0.132$  and  $a_3 = 2.7a = 0.356$ . The second regime has exponent  $\gamma_2 \approx 0.54$  and pre-factor  $a_2 = a(Ra_{low})^{\gamma - \gamma_2}$ . The Rayleigh number  $Ra_{high}$  that marks the border between the second and third regimes can then be determined as:

$$Ra_{high} = Ra_{low} 2.7^{\frac{1}{\gamma_2 - \gamma}} \quad (4)$$

The transition from the first regime (smooth regime) to a regime with enhanced heat transfer when the boundary layer thickness is equal to the roughness height (at  $Ra = Ra_{low}$ ) has some degree of universality. It is confirmed in a large number of exper-

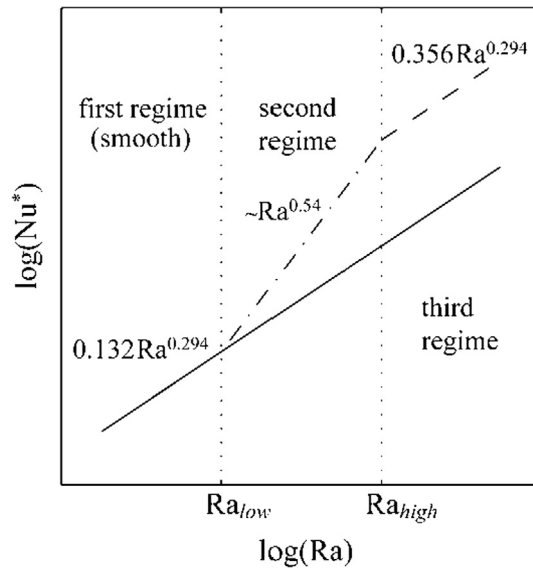


Fig. 3d. Model for Nusselt-Rayleigh relation for rough walls.

imental and numerical studies for different types of roughness. The occurrence of the third regime (for  $Ra > Ra_{high}$ ) with the increase of the Nusselt number by a constant factor (compared to the Nusselt number for the smooth case) appears to be less universal. For example Tisserand et al. [10], Roche et al. [9] and Salort et al. [27] did not observe a saturation effect in their experiments. However, this may have been the result of considering a too small range of Rayleigh numbers since the second regime is quite wide in terms of Rayleigh number. For example,  $Ra_{high}/Ra_{low} = 2.7^{4.07} \approx 57$  in the present experiment. Xie and Xia [13] reported on the three different regimes and showed that the value of the exponent in the second regime depends on the geometry, or more specifically, on the aspect ratio  $\lambda$  which is defined as the ratio of the height and the base width of the roughness element. They have reported a value of 0.43 for the case with  $\lambda = 1$ . Rusaouën et al. [14] take the exponent in the second regime as 0.5 and assume that the pre-factor varies with the ratio  $h/H$ . In several other experiments (e.g. Roche et al. [9] and Tisserand et al. [10]) it is also observed that the value of the exponent in the second region is close to 0.50, which is characteristic for the ultimate regime predicted by Kraichnan [28]. However, the results of the 2D numerical simulations reported by Zhu et al. [30] showed that an exponent with a value of 0.5 does not indicate the onset of the ultimate regime because the value of the exponent decreases with a further increase of the Rayleigh number resulting in the third regime.

### 3.3. Results from the suspended TLC recordings

The specifications of the useful temperature range of the TLCs effectively set the temperatures of the top and bottom plates (see Section 2.2). The red start is at 19.7 °C and the upper clearing point is around 28.3 °C. These limits result in a Rayleigh number of  $Ra = 6.9 \times 10^7$  for experiments in the small cells. The corresponding Prandtl-number-corrected Nusselt numbers are  $Nu^* = 27.9$  and  $Nu^* = 52.1$  for the smooth cell and the rough cell, respectively. The recordings of the TLC tracer images consist of a series of  $2.5 \times 10^4$  sequential snapshots acquired at a frame rate of 7.9 Hz for each cell. The measurement time of 3165 s corresponds to 1558 free fall time scales  $T_{ff}$  computed as  $T_{ff} = (H/(\alpha g \Delta T))^{1/2} = 2.03$  s.

Figs. 4a and 4b show snapshots from TLC recordings in the smooth and rough cells, respectively. The instantaneous tempera-

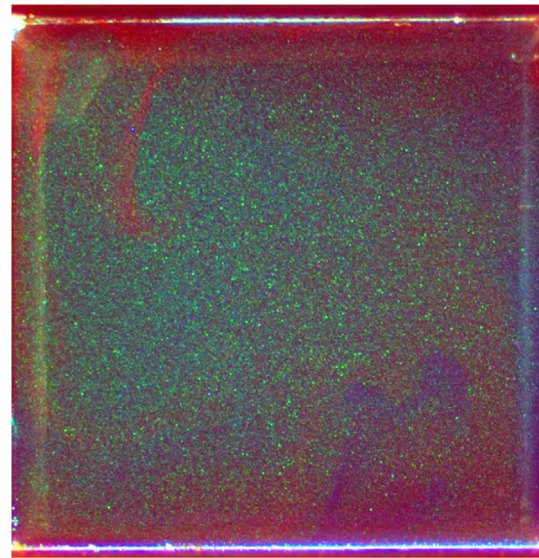


Fig. 4a. Snapshot from TLC recording in the (water-filled, small) smooth cell at  $Ra = 6.9 \times 10^7$ .

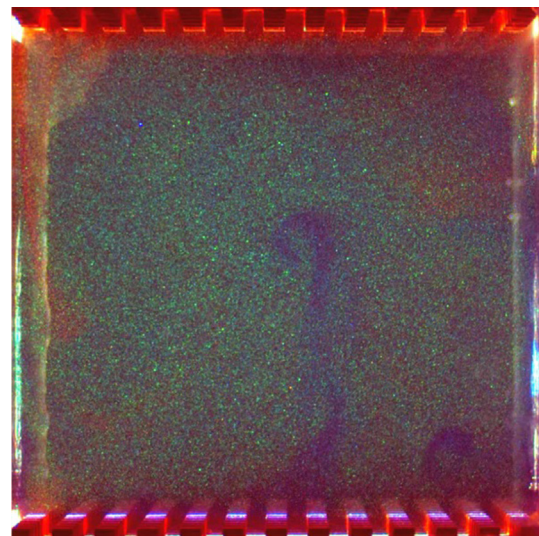


Fig. 4b. Snapshot from TLC recording in the (water-filled, small) cell with 3 mm roughness at  $Ra = 6.9 \times 10^7$ .

ture fields in the two cells are quite different. First, individual plumes that erupt from the horizontal boundary layers in the smooth cell are generally unable to traverse the core of the cell. These plumes diffuse rather quickly in the core. The plumes in the smooth cell reach the opposing horizontal wall mainly by moving with the large scale circulation (LSC) along the periphery of the walls while the core is relatively quiescent and well-mixed in agreement with earlier results reported by e.g. Xia et al. [29]. Plumes (or groups of plumes) that move with the LSC are also observed in the rough cell. The most important difference between the smooth and rough cells is that in the latter the plumes are much stronger. As a result, these individual plumes are able to traverse the core and then impinge on the opposing horizontal wall, as illustrated in Fig. 4b. This phenomenon is thought to be a main reason for the increased heat transfer in the rough cell. Close inspection of the TLC recordings near, say, the bottom wall shows that the increased strength of the plumes is directly related to the prolonged accumulation of hot fluid in the relatively quiescent

spaces in between the roughness elements. As a consequence, a relatively large amount of hot fluid is released when a plume erupts from the thermal boundary layer on a rough wall. Secondly, it is observed that the plume behaviour in the bottom left corner and in the top right corner is different in both cells. This will be discussed in the next section.

### 3.4. Results from the PIV measurements

The TLC recordings were also used to determine the flow fields inside the smooth and rough cells. Figs. 5a and 5b depict the mean velocity fields for the smooth cell and the rough cell, respectively. In both cells the highest mean velocities are concentrated along the walls, whilst the centre region (core) is characterized by much lower mean velocities thus indicating the existence of a LSC. The mean flow in the smooth cell is quite symmetric with an oval-shaped LSC very similar to what has been reported by Xia et al. [29]. The oval-shaped LSC in the rough cell is slightly flatter and its core is somewhat displaced to the upper left corner.

In each cell there are two secondary rolls in the mean flow field, one in the bottom left corner and one in the top right corner. The secondary rolls are counter-rotating with respect to the direction of the LSC. The area-averaged mean velocity magnitude in the rough cell is approximately 12% larger than in the smooth cell. The higher velocity may increase the heat transfer, but this rather small difference in mean velocity cannot explain the large increase in the measured Nusselt number. Interestingly, the dynamical behaviour of the velocity fields in both cells is very different. This is illustrated in Figs. 6a and 6b which show the turbulence kinetic energy, defined here as  $k = 1/2(\overline{u'^2} + \overline{w'^2})$ , for the smooth and rough cell, respectively. In the expression for  $k$ , the symbols  $u'$  and  $w'$  represent the deviation from the mean velocity components  $\bar{u}$  and  $\bar{w}$ . Clearly, the intensity of the turbulent velocity fluctuations is much higher (approximately 45%) in the rough cell. The secondary rolls play an important role in the increase of the turbulence kinetic energy. Consistent with observations from the TLC recordings, the rolls are formed in the corners where the LSC attaches to the top/bottom plates. Plumes that erupt from the por-

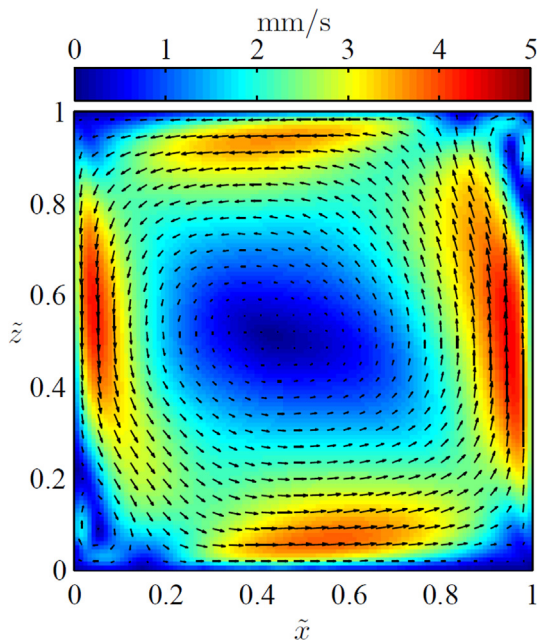


Fig. 5a. The mean velocity field in the (water-filled, small) smooth cell at  $Ra = 6.9 \times 10^7$ .

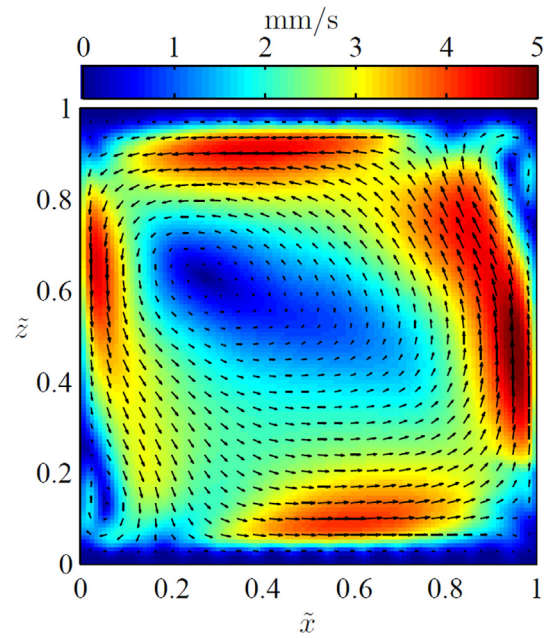


Fig. 5b. The mean velocity field in the (water-filled, small) cell with 3 mm roughness at  $Ra = 6.9 \times 10^7$ .

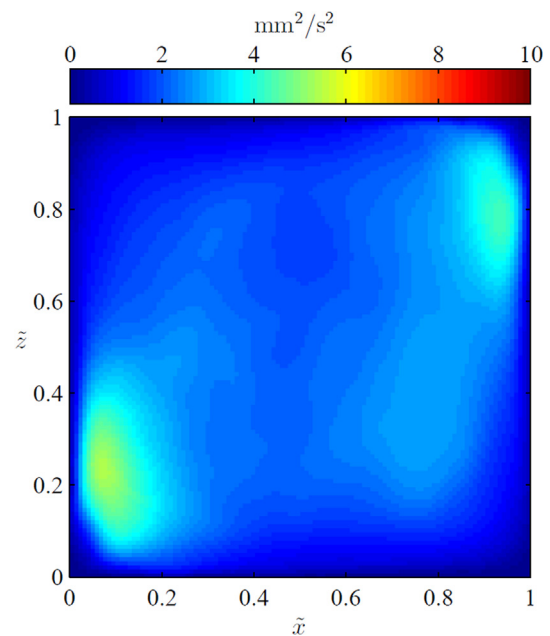
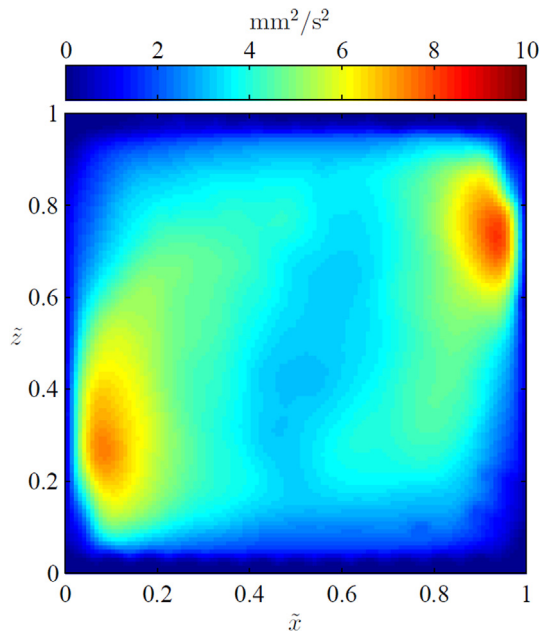


Fig. 6a. The turbulence kinetic energy in the (water-filled, small) smooth cell at  $Ra = 6.9 \times 10^7$ .

tion of the thermal boundary layer in between the (unsteady) attachment point and the corner regularly tend to flow against the direction of the LSC. This mechanism is present in both cells, but the temporary flow of (groups of) plumes against the LSC is much stronger in the rough cell to such an extent that these plumes are able to reach the opposing horizontal plate. When a group of, say, hot plumes from the secondary roll in the lower left corner of the cell move against the LSC towards the top wall, the downward motion of the cold plumes along the vertical side wall is interrupted. This stimulates the release of large cold plumes from the top plate (instead of moving with the LSC along the top plate followed by a descent along the vertical side wall) which sub-



**Fig. 6b.** The turbulence kinetic energy in the (water-filled, small) cell with 3 mm roughness at  $Ra = 6.9 \times 10^7$ .

sequently traverse the core of the cell and then impinge on the bottom wall. The size and strength of the secondary rolls in the rough cell vary strongly with time (much more than in the smooth cell). Maximum size and strength are reached at the moment when the plumes are moving against the LSC towards the opposing wall, while the secondary roll practically disappears at the end of such an event. The strong variation in the growth and decay phases of the secondary rolls produces the higher turbulence kinetic levels in the corners of the cell.

We have thus identified a second mechanism for (groups of) plumes to impinge on the opposing plate, apart from the mechanism in which individual plumes traverse the core as described in Section 3.3. Since heat transfer coefficients for impinging flows are generally higher than for wall parallel flows, it is expected that the impingement of plumes on the horizontal plates enhances the heat transfer compared to the case where only (groups of) plumes move with the LSC from one horizontal plate to another. Also, hot fluid that has accumulated in the spaces in between the cubes, especially in the wakes that form downstream of the cubes, cannot be easily washed out by the LSC (see Salort et al. [27] and Liot et al. [31]). Direct impingement may be more effective in removing heat from the spaces in between cubes including the wake zones.

#### 4. Conclusions

An experimental study into the effects of surface roughness (in the form of an inline array of copper cubes) on the flow and heat transfer in Rayleigh-Bénard (R-B) convection was carried out. The experiments in the smooth R-B cells resulted in a relation between the Nusselt number  $Nu$  and the Rayleigh number  $Ra$  in the form of a power law:  $Nu = a Ra^\gamma$  with pre-factor  $a = 0.132$  and exponent  $\gamma = 0.294$  for  $Ra$ -numbers ranging between  $10^7$  and  $10^{10}$ . The study shows that three different regimes exist for the R-B cells with rough top and bottom walls, in line with earlier findings. In the first regime (smooth regime) the  $Nu$ - $Ra$  relation equals that of the smooth cell. In the second regime, the  $Nu$ - $Ra$  relation deviates from that in the smooth regime through a higher value of the exponent (0.54). In the third regime the value of the exponent is very similar to that for the smooth regime, but the value of pre-factor is

significantly higher (0.356). The boundary between the smooth regime and the second regime occurs where the height of the cubes  $h$  is equal to the thermal boundary layer thickness  $\delta_\theta$ . This corresponds to a Rayleigh number  $Ra_{low} = \left( H / (2ahPr^{0.05}) \right)^{1/\gamma}$ , where  $Pr$  is the Prandtl number of the working fluid.

Recordings of encapsulated thermochromic liquid crystal tracer particles were used to visualise the temperature distribution and determine the velocity fields (by using particle image velocimetry) in the smooth and rough cells for  $Ra = 6.9 \times 10^7$  (in the second regime with enhanced heat transfer). In both cells the flow fields exhibit a large scale circulation along the periphery of the cell with the velocity magnitude in the rough cell about 12% higher than in the smooth cell. The turbulence kinetic energy level in the rough cell is about 45% higher than in the smooth cell. The recordings of the thermochromic liquid crystals showed that hot fluid accumulated in the quiescent regions in between the cubical roughness elements, which resulted in the formation of strong plumes that can traverse the core of the cell and directly impinge on the opposing horizontal plate. Strong plumes originating from the secondary rolls in the lower left and upper right corners of the cell were also able to reach the opposing horizontal plates. These impingement phenomena are thought to be responsible for the enhanced heat transfer in the rough cell.

#### Declaration of Competing Interest

The authors declared that there is no conflict of interest.

#### References

- [1] G. Ahlers, S. Grossmann, D. Lohse, Heat transfer and large scale dynamics in turbulent Rayleigh-Bénard convection, *Rev. Mod. Phys.* 81 (No. 2) (2009).
- [2] D. Lohse, K.-Q. Xia, Small-scale properties of turbulent Rayleigh-Bénard convection, *Annu. Rev. Fluid Mech.* 42 (2010) 335–364.
- [3] F. Chillà, J. Schumacher, New perspectives in turbulent Rayleigh-Bénard convection, *Eur. Phys. J. E* 35 (2012) 58.
- [4] R.J.A.M. Stevens, E.P. van der Poel, S. Grossmann, D. Lohse, The unifying theory of scaling in thermal convection: the updated prefactors, *J. Fluid Mech.* 730 (2013) 295–308.
- [5] S. Grossmann, D. Lohse, Scaling in thermal convection: a unifying theory, *J. Fluid Mech.* 407 (2000) 27–56.
- [6] Y.-B. Du, P. Tong, Turbulent thermal convection in a cell with ordered rough boundaries, *J. Fluid Mech.* 407 (2000) 57–84.
- [7] Y. Shen, P. Tong, K.-Q. Xia, Turbulent convection over rough surfaces, *Phys. Rev. Lett.* 76 (1996) 908–911.
- [8] X.-L. Qiu, K.-Q. Xia, P. Tong, Experimental study of velocity boundary layer near a rough conducting surface in turbulent natural convection, *J. Turbul.* 6 (2005) N30.
- [9] P.-E. Roche, B. Castaing, B. Chabaud, B. Hébral, Observation of the 1/2 power law in Rayleigh-Bénard convection, *Phys. Rev. E* 63 (2001) 045303.
- [10] J.-C. Tisserand, M. Creysseels, Y. Gasteuil, H. Pabiau, M. Gibert, B. Castaing, F. Chillà, Comparison between rough and smooth plates within the same Rayleigh-Bénard cell, *Phys. Fluids* 23 (2011) 015105.
- [11] S. Ciliberto, C. Laroche, Random roughness of boundary increases the turbulent convection scaling exponent, *Phys. Rev. Lett.* 82 (1999) 3998–4001.
- [12] E. Villermaux, Transfer at rough sheared interfaces, *Phys. Rev. Lett.* 81 (1998) 4859–4862.
- [13] Y.-C. Xie, K.-Q. Xia, Turbulent thermal convection over rough plates with varying roughness geometries, *J. Fluid Mech.* 825 (2017) 573–599.
- [14] E. Rusaouën, O. Liot, B. Castaing, J. Salort, F. Chillà, Thermal transfer in Rayleigh-Bénard cell with smooth or rough boundaries, *J. Fluid Mech.* 837 (2018) 443–460.
- [15] O. Shishkina, C. Wagner, Modelling the influence of wall roughness on heat transfer in thermal convection, *J. Fluid Mech.* 686 (2011) 568–582.
- [16] S. Wagner, O. Shishkina, Heat flux enhancement by regular surface roughness in turbulent thermal convection, *J. Fluid Mech.* 763 (2015) 109–135.
- [17] X. Zhu, R. Ostilla-Mónico, R. Verzicco, D. Lohse, Direct numerical simulation of Taylor-Couette flow with grooved walls: torque scaling and flow structure, *J. Fluid Mech.* 794 (2016) 746–774.
- [18] P.-E. Roche, B. Castaing, B. Chabaud, B. Hébral, J. Sommeria, Side wall effects in Rayleigh Bénard experiments, *Eur. Phys. J. B – Condens. Matter Complex Syst.* 24 (3) (2001) 405–408.
- [19] R.J. Adrian, J. Westerweel, *Particle Image Velocimetry*, Cambridge University Press, 2011, ISBN 978-0-521-44008-0.
- [20] A.T. Hjelmfelt, L.F. Mockros, Motion of discrete particles in a turbulent fluid, *Appl. Sci. Res.* 16 (1) (1966) 149–161.

- [21] D. Dabiri, Digital particle image thermometry/ velocimetry: a review, *Exp. Fluids* 46 (2009) 191–241.
- [22] N. Abdullah, A. Talib, A. Jaafar, M. Salleh, W.T. Chong, The basics and issues of thermochromic liquid crystal calibrations, *Exp. Therm. Fluid Sci.* 34 (2010) 1089–1121.
- [23] A. Günther, Ph. Rudolf von Rohr, Influence of the optical configuration on temperature measurements with fluid-dispersed TLCs, *Exp. Fluids* 32 (2002) 533–541.
- [24] K.-Q. Xia, S. Lam, S.-Q. Zhou, Heat flux measurements in high Prandtl-number turbulent Rayleigh-Bénard convection, *Phys. Rev. Lett.* 88 (6) (2002) 064501.
- [25] A. Belmonte, A. Tilgner, A. Libchaber, Temperature and velocity boundary layers in turbulent convection, *Phys. Rev. E* 50 (1) (1994) 269–279.
- [26] G. Stringano, G. Pascazio, R. Verzicco, Turbulent thermal convection over grooved plates, *J. Fluid Mech.* 557 (2006) 307–336.
- [27] J. Salort, O. Liot, E. Rusaouen, F. Seychelles, J.-C. Tisserand, M. Creyssels, B. Castaing, F. Chillà, Thermal boundary layer near roughnesses in turbulent Rayleigh-Bénard convection: flow structure and multistability, *Phys. Fluids* 26 (2014) 015112.
- [28] R.H. Kraichnan, Turbulent thermal convection at arbitrary Prandtl number, *Phys. Fluids* 5 (11) (1962) 1374–1389.
- [29] K.-Q. Xia, C. Sun, S.-Q. Zhou, Particle image velocimetry measurements of the velocity field in turbulent thermal convection, *Phys. Rev. E* 68 (2003) 066303.
- [30] X. Zhu, R.J.A.M. Stevens, R. Verzicco, D. Lohse, Roughness-facilitated local  $1/2$  scaling does not imply the onset of the ultimate regime of thermal convection, *Phys. Rev. Lett.* 119 (2017) 154501.
- [31] O. Liot, J. Salort, R. Kaiser, R. du Puits, F. Chillà, Boundary layer structure in a rough Rayleigh-Bénard cell filled with air, *J. Fluid Mech.* 786 (2016) 275–293.